

SCIENTIFIC REPORTS

OPEN

Crystal structure investigation of $\text{La}_{5.4}\text{W}_{1-y}\text{Mo}_y\text{O}_{12-\delta}$ for gas separation by high-resolution transmission electron microscopy

K. Ran^{1,2}, W. Deibert³, M. E. Ivanova³, W. A. Meulenber^{3,4} & J. Mayer^{1,2}

Lanthanum tungstate (LWO) and LWO with 20 at.% and 35 at.% molybdenum substituting tungsten were prepared by the Pechini method. Phase purity and successful Mo substitution inside these dense LWO membrane materials were confirmed by conventional and high resolution transmission electron microscopy techniques. The split of La_2/W_2 site by around 0.3 Å was proven. Extra reflections show up in the diffraction patterns from Mo-substituted LWO, and together with simulations, these reflections were recognized as forbidden reflections in a non-substituted LWO system, while the extinction rules are broken by Mo substitution due to the different scattering factors of W and Mo. Energy-dispersive X-ray chemical mapping allowed direct visualization of individual atomic columns, and revealed that all Mo is located at the W_1 sites in the Mo-substituted LWO. Moreover, the diffuse scattering in diffraction patterns provides direct evidence of short range clustering of oxygen vacancies and could be further related to the oxygen conduction of the LWO membranes.

Mixed proton-electron conductors are promising gas separation membranes and have attracted great research interests^{1–5}. Comparing with membranes based on precious metal alloys or polymers, ceramics-based membranes offer certain advantages, such as better thermal and mechanical stability, long-term durability, as well as cost effectiveness. So far, the most widely studied oxide-based ceramic materials are perovskites, where several acceptor-doped cerates^{6–8} and zirconates^{9,10} show good ambipolar conductivity and relatively high hydrogen flux. However, stability of the cerates in CO_2 , H_2O and S-containing atmospheres and the low grain-boundary conductivity of zirconates always present a critical issue with respect to their application.

As an alternative candidate, much attention has been recently given to lanthanum tungstate (LWO)^{11–13}. A general formula to describe LWO is $\text{La}_{28-x}\text{W}_{4+x}\text{O}_{54+\delta}\text{V}_{2-\delta}$, where x is the amount of tungsten sitting on a lanthanum site, which in turn determines how many oxygen vacancies (v) are in the structure as inherent defects^{14,15}. The LWO holds appreciable mixed proton and electron conductivity, thermal and hydrothermal stability as well as chemical stability in reducing and water-containing atmospheres at elevated temperatures. It has been pointed out that single-phase LWO can be prepared at 1500 °C with a La/W ratio in the window between 5.3 and 5.7^{16,17}. Outside this compositional range, segregation of either La_2O_3 or $\text{La}_6\text{W}_2\text{O}_{15}$ was found. While the formation of La_2O_3 is accompanied by a volume expansion that destroys the membrane in a relatively short time, the presence of $\text{La}_6\text{W}_2\text{O}_{15}$ leads to intensive crack formation and complete disintegration of the membrane¹⁸.

At low and intermediate temperatures, LWO is a relatively pure proton conductor caused by hydration of intrinsic oxygen vacancies. For its application as gas separation membrane at higher temperatures, where mixed conductivity is required, electronic conductivity becomes the main limiting factor. In order to optimize the LWO performance, enhancing its electronic conductivity while retaining similar proton conductivity would be desired. Among many studies, partial substitution of tungsten by a more reducible cation such as molybdenum or rhenium was reported to serve this purpose^{11,15,17,19–21}. For example, the Mo-substituted LWO exhibits a predominantly n-type electronic and oxygen-ionic conductivity in the temperature range 500–800 °C, while its stability

¹Central Facility for Electron Microscopy GFE, RWTH Aachen University, 52074, Aachen, Germany. ²Ernst Ruska-Centre for Microscopy and Spectroscopy with Electrons ER-C, Forschungszentrum Jülich GmbH, 52425, Jülich, Germany. ³Institute of Energy and Climate Research IEK-1, Forschungszentrum Jülich GmbH, 52425, Jülich, Germany. ⁴Faculty of Science and Technology, Inorganic Membranes, University of Twente, 7500 AE, Enschede, The Netherlands. Correspondence and requests for materials should be addressed to K.R. (email: ran@gfe.rwth-aachen.de)

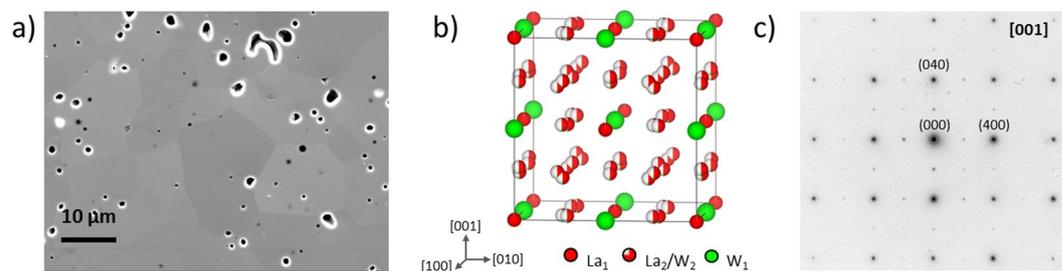


Figure 1. Structural information of LWO. (a) Cross-section SEM image of LWO-Mo₀₀. (b) One unit cell of the average LWO model. Oxygen is not shown here. (c) Diffraction pattern from LWO-Mo₀₀ along [001] zone axis, indexed by the model in (b).

in reducing atmospheres was confirmed by various characterization methods^{11,21}. Meanwhile, reducing the LWO membrane thickness is considered as an alternative way to improve its performance, and asymmetric membrane structures using porous MgO and LWO as substrates were prepared^{22–24}.

In spite of extensive studies on the conducting properties of LWO or Mo/Re-substituted LWO and several reports determining their structural models by neutron and X-ray diffraction (XRD)^{14,15,19,25,26}, only a few attempts were made to characterize the mixed conductors using transmission electron microscopy (TEM) with atomic resolution. At local scale, a certain degree of oxygen vacancy ordering was revealed by electron diffraction in La_{5.7}WO_{12–δ} in contrast to La_{5.3}WO_{12–δ}, as lower tungsten content and therefore more oxygen vacancies in La_{5.7}WO_{12–δ} is expected¹⁴. Phase purity and structural stability of La_{5.5}WO_{12–δ} and La_{5.5}W_{0.8}Mo_{0.2}O_{12–δ} were confirmed by TEM imaging before and after H₂ permeation test²¹. Combining electron diffraction and high resolution TEM, nanodomains with an incipient superstructure were reported in La_{28–γ}(W_{0.6}Mo_{0.4})_{4+γ}O_{54+δ}, and when the Mo content goes higher, a new phase with rhombohedral structure was proposed^{15,20}.

Here we performed a comprehensive TEM study to characterize the crystal structure of Mo-substituted LWO at atomic scale. The LWO membrane materials with nominal La/W ratio of 5.4 (in atomic percent) were prepared by the Pechini method²⁷, where nominally 20 at.% and 35 at.% W was substituted by Mo respectively. Various techniques were employed, including high-angle annular dark-field (HAADF) imaging, energy-dispersive X-ray (EDX) chemical mapping, electron diffraction and simulations of HAADF images and diffraction patterns. The main focus is to precisely locate the Mo dopant and understand the LWO crystal structure before and after Mo substitution. The structural information revealed in this study has the potential to be further correlated with the gas separation performance of the Mo-substituted LWO membrane and could provide valuable information to achieve a better system with improved mixed conductivity, mechanical stability and tolerance for the harsh working environment.

Results and Discussion

Three types of sintered pellets, pure LWO, LWO with nominally 20 at.% and 35 at.% of W replaced by Mo (LWO-Mo₀₀, LWO-Mo₂₀ and LWO-Mo₃₅) were prepared and studied in this work. An even higher Mo content was found to degrade the membranes' mechanical stability in preliminary experiments, and is therefore excluded from this study. The as-sintered pellets of the three types were first analyzed by XRD, in which all of them were proven to be phase pure within the experimental detection limit (Supplementary Fig. S1). Starting from the pellets, cross-section scanning electron microscope (SEM) samples were firstly prepared, which were used later for cutting lamellas by the focused ion beam (FIB) technique.

Microstructure of non-substituted LWO, LWO-Mo₀₀. Figure 1a shows a cross-section SEM image from the LWO-Mo₀₀. Compact grains with irregular shapes and clean boundaries are visible. The grain size ranges from several micrometers up to tens of micrometers. Individual pores appearing as dark dots with mostly shiny edges, can be located both inside the grains and at the grain boundaries, without clear preference. The shiny edges are a result of charging, as carbon coating is less effective around the pores. Based on the SEM EDX measurement, no Mo was detected in LWO-Mo₀₀ (Supplementary Figs S2 and S3). Thus, an average LWO structural model with a cubic fluorite-related structure²⁸ belonging to the space group *Fm $\bar{3}$ m* (as will be discussed later), was employed to describe the LWO-Mo₀₀ structure. As shown in Fig. 1b, W₁ and La₁ atoms form a face-centered cubic (fcc) lattice. The nearest W₁ neighbors are linked by a La₂ site, which is split into two sites and thus each one is only half occupied. An additional W atom (W₂) sits on one of the La₂ sites to stabilize the LWO phase. A diffraction pattern from a single LWO-Mo₀₀ grain is shown in Fig. 1c, which can be fully indexed as recorded along [001] zone axis, based on the model shown in Fig. 1b.

LWO-Mo₂₀ and LWO-Mo₃₅ by electron diffraction. Both the LWO-Mo₂₀ and LWO-Mo₃₅ show compact grains with similar sizes, clean grain boundaries and randomly distributed pores as LWO-Mo₀₀ (Supplementary Fig. S2). SEM EDX results confirm the successful Mo substitution in both materials, and the content of Mo determined by electron probe microanalysis (EPMA) shows remarkable consistence with the nominal values (Supplementary Table S1). Moreover, the porosities among the three membrane materials are noticed to decrease as the Mo content increases (Supplementary Fig. S2).

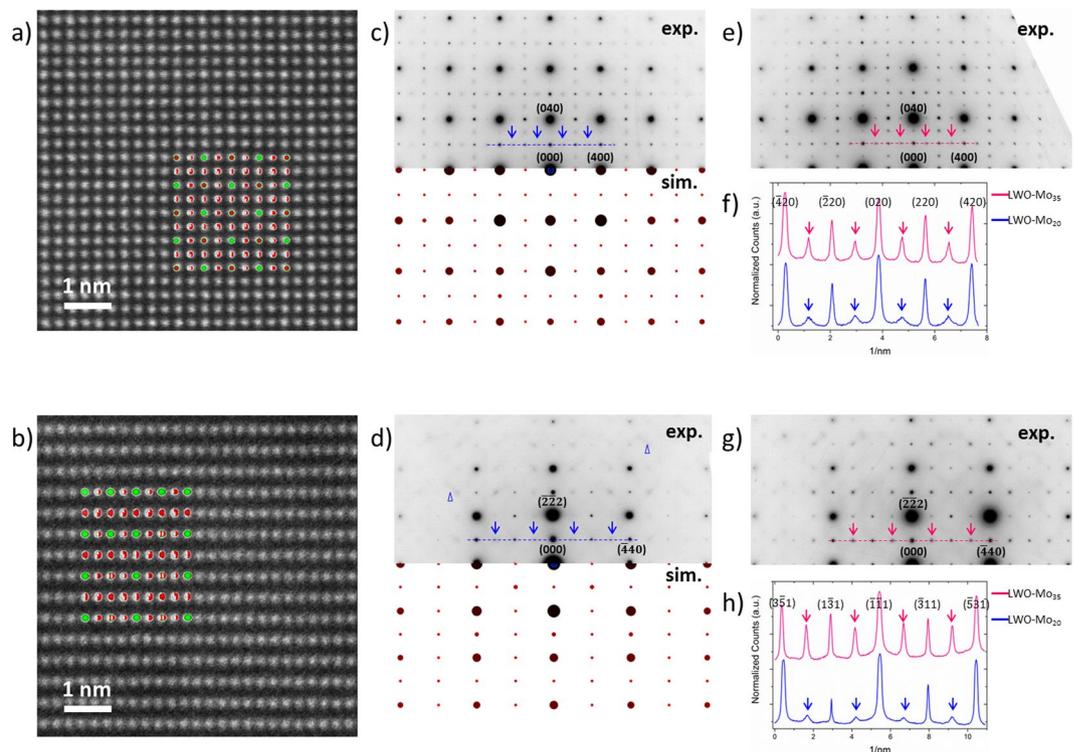


Figure 2. (a,b) HAADF images of LWO-Mo₂₀ recorded along [001] and [112]. Insets are the average LWO model oriented correspondingly. (c,d) Comparison of the experimental pattern from LWO-Mo₂₀ (upper part, exp.), and the simulated pattern (lower part, sim.) based on the average LWO model, along [001] and [112] zone axis respectively. (e) Diffraction pattern from LWO-Mo₃₅ recorded along [001]. (f) Intensity profiles extracted from the dashed lines in (c) and (e). The blue/pink arrows mark the same reflections as the blue/pink arrows in (c)/(e). (g) Diffraction pattern from LWO-Mo₃₅ recorded along [112]. (h) Intensity profiles extracted from the dashed lines in (d) and (g). The blue/pink arrows mark the same reflections as the blue/pink arrows in (d)/(g).

Figure 2a–d show HAADF images and diffraction patterns from LWO-Mo₂₀, along [001] and [112] directions, respectively. The average LWO models are oriented correspondingly and placed as insets in Fig. 2a,b. Figure 2c,d compares the experimental (upper part, exp.) and simulated (lower part, sim.) diffraction patterns based on the average LWO model. While the HAADF images can still be qualitatively understood by the model, both experimental diffraction patterns show a distinct discrepancy from the simulations in Fig. 2c,d. In general, diffuse scattering is noticeable, as suggested by the blue triangles in Fig. 2d. In addition, not all the reflections can be indexed by the average LWO model, and some of them are marked by the blue arrows in Fig. 2c,d. For comparison, diffraction patterns were recorded from LWO-Mo₃₅ along [001] and [112] as well, see Fig. 2e,g. Similar diffuse scattering and extra reflections show up in the LWO-Mo₃₅ patterns. Along the dashed line in Fig. 2c,e, intensity profiles are extracted and plotted in Fig. 2f. For both LWO-Mo₂₀ and LWO-Mo₃₅, extra reflections arise at equal positions (midpoint between two indexed spots), and become apparently stronger in LWO-Mo₃₅ than in LWO-Mo₂₀. Intensity profiles are compared between the two [112] patterns as well in Fig. 2h. Again, extra reflections are noticed at corresponding positions, and show higher intensity in LWO-Mo₃₅ than in LWO-Mo₂₀. Such a behavior is consistently observed in the diffraction patterns from LWO-Mo₂₀ and LWO-Mo₃₅ along other zone axes as well (Supplementary Fig. S4).

LWO-Mo₂₀ and LWO-Mo₃₅ by EDX chemical mapping. Atomic resolution EDX chemical mapping was then carried out for all samples, and the results from LWO-Mo₂₀ along the [001] zone axis are shown in Fig. 3. Figure 3a–d depict the simultaneously recorded HAADF image, and maps from the La *L* line, W *L* line and Mo *L* line, extracted with selected energy windows, respectively. Clearly, direct visualization of La and W atomic columns is possible. In Fig. 3b, the La is noticed to occupy each atomic column, but recognized with two different intensities. Each column with a relatively lower intensity and thus lower La content stays at the center of a square defined by eight other columns with higher intensity and thus higher La content, in Fig. 3b marked by the dashed circle and square. In contrast, the local maxima in the W map are all located at the less preferred La sites. The top circle in Fig. 3c is placed at the same position as the circle in Fig. 3b, and this coincidence is more evident in the mixed La and W map in Fig. 3e. The Mo map in Fig. 3d shows a quite low intensity due to its low concentration. However, the coincidence between local maxima of Mo and several W local maxima can still be determined unambiguously, as indicated by the circles which are placed at equal positions in Fig. 3c,d. Referring to the average LWO unit cell, there are two types of atomic columns (A and B) when viewed along [001] direction, as shown in Fig. 3f. The type A column contains one La₁ and one W₁ atom corresponding to the less preferred La

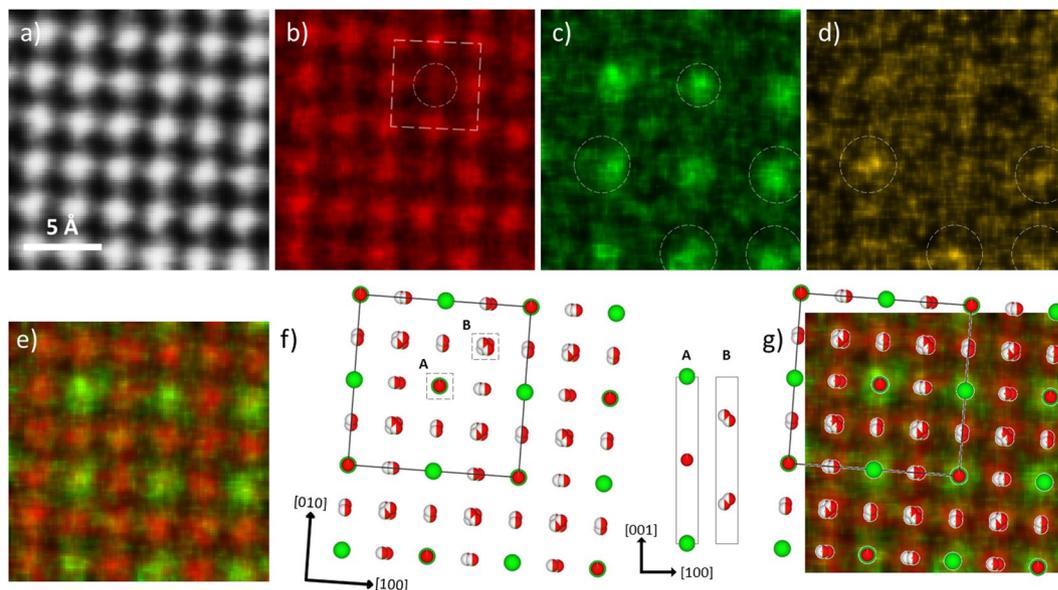


Figure 3. EDX chemical mapping of LWO-Mo₂₀. (a–d) Simultaneously recorded HAADF image and maps from La *L* line, W *L* line and Mo *L* line from LWO-Mo₂₀ along [001] zone axis. (e) Mixed La and W map. (f) The average LWO model oriented along [001], and the solid square defines one unit cell. Two types of atomic columns (A and B) are sketched on the right by vertically flipping the model. (g) Comparison between the average LWO model and the mixed La and W map.

sites (local maxima of W), and the type B consists of two split La₂/W₂ sites, corresponding to the more preferred La sites. The comparison in Fig. 3g between the average LWO model and the mixed La and W map, shows a good agreement, implying that the Mo substitution doesn't change the LWO crystal structure.

Along the [101] zone axis, EDX spectrum imaging was also applied to LWO-Mo₃₅. Figure 4a–d show the simultaneously recorded HAADF image, and maps from the La *L* line, W *L* line and Mo *L* line. The La map in Fig. 4b shows again a La occupation of all atomic columns but with two types of intensities. The less preferred La site stays at the center of a rhombohedron defined by eight more preferred La sites, as indicated by the circle and rhombohedron in Fig. 4b. The less preferred La sites, local maxima of W and local maxima of Mo coincide with each other, and one example is indicated by the circles in Fig. 4b–d. Comparing with Fig. 3d, the local maxima of Mo in Fig. 4d show a clearly higher visibility and a more even coverage of the W₁ sites. Three types of atomic columns are indicated in the average LWO model along [101] projection, as sketched in Fig. 4f. In addition to the aforementioned type B in Fig. 3f, two other types are expected. The type A' column has a W₁ and a split La₂/W₂. Similarly, the two atomic sites in type C columns are occupied by a La₁ and a split La₂/W₂ respectively. However, the difference between type B and C is too small to be distinguished by EDX mapping, and therefore only two kinds of intensity are noticed in Fig. 4b. Again, the average LWO model and the mixed La and W map show a good agreement in Fig. 4g.

Understanding the diffraction pattern. The HAADF images from both LWO-Mo₂₀ and LWO-Mo₃₅ show a good agreement with the average LWO model, yet provide limited information about the Mo distribution. As a complementary technique, EDX chemical mapping provides direct evidence on Mo replacing W, and thus suggests a substituted model for further study of the extra reflections in Fig. 2. Figure 5a,b are the HAADF image and diffraction pattern from LWO-Mo₃₅ along the [101] zone axis. The image quality in Fig. 5a was improved through averaging by an iterative rigid alignment algorithm and smoothing by a nonlinear filtering algorithm²⁹. A detailed process is described in the Supplementary Fig. S5. An average LWO model oriented correspondingly together with a simulated HAADF image based on the model are shown as insets in Fig. 5a. The diffraction pattern was simulated based on the same model, see Fig. 5c. Between the simulated and experimental image in Fig. 5a, no significant difference is noticed. However, when comparing the diffraction patterns in Fig. 5b,c, extra reflections show up again in the experimental pattern. Several extra reflections are marked by the arrows in Fig. 5b, and indexed based on their positions. Replacing the center W atom by a Mo atom, Fig. 5d suggests a feasible model for the Mo-substituted LWO, where the pristine LWO lattice is kept and a Mo/(W + Mo) ratio around 25 at.% is reached. Diffraction pattern was then simulated based on this substituted model along [101], see Fig. 5e. As marked by the arrows, similar extra reflections as in Fig. 5b exist in Fig. 5e.

To understand these extra reflections, the average LWO model can be further simplified as two sets of fcc lattices of La₁ and W₁, which are shifted by $\bar{a}/2$ from each other. The La₂/W₂ sites barely show influence on the experimentally observed extra reflections, as similar diffraction patterns were simulated, based on models with and without La₂/W₂ sites (Supplementary Fig. S6). In addition, given the low occupancy of W at the La₂/W₂ sites, the chance that a Mo atom replaces a W atom at La₂/W₂ sites is even lower and thus can be ignored. This assumption is also supported by the chemical mapping in Figs 3 and 4, where local maxima of Mo were only located at

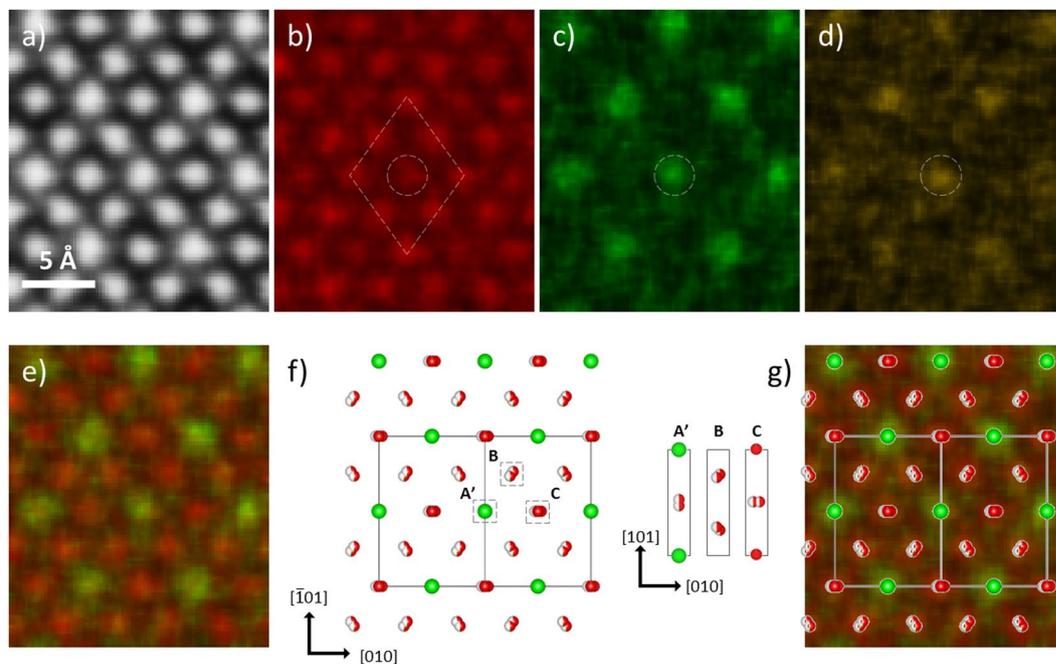


Figure 4. EDX chemical mapping of LWO-Mo₃₅. (a–d) Simultaneously recorded HAADF image and maps from La *L* line, W *L* line and Mo *L* line from LWO-Mo₃₅ along [101] zone axis. (e) Mixed La and W map. (f) The average LWO model oriented along [101], and the solid square defines one unit cell. Three types of atomic columns (A', B and C) are sketched on the right by vertically flipping the model. (g) Comparison between the average LWO model and the mixed La and W map.

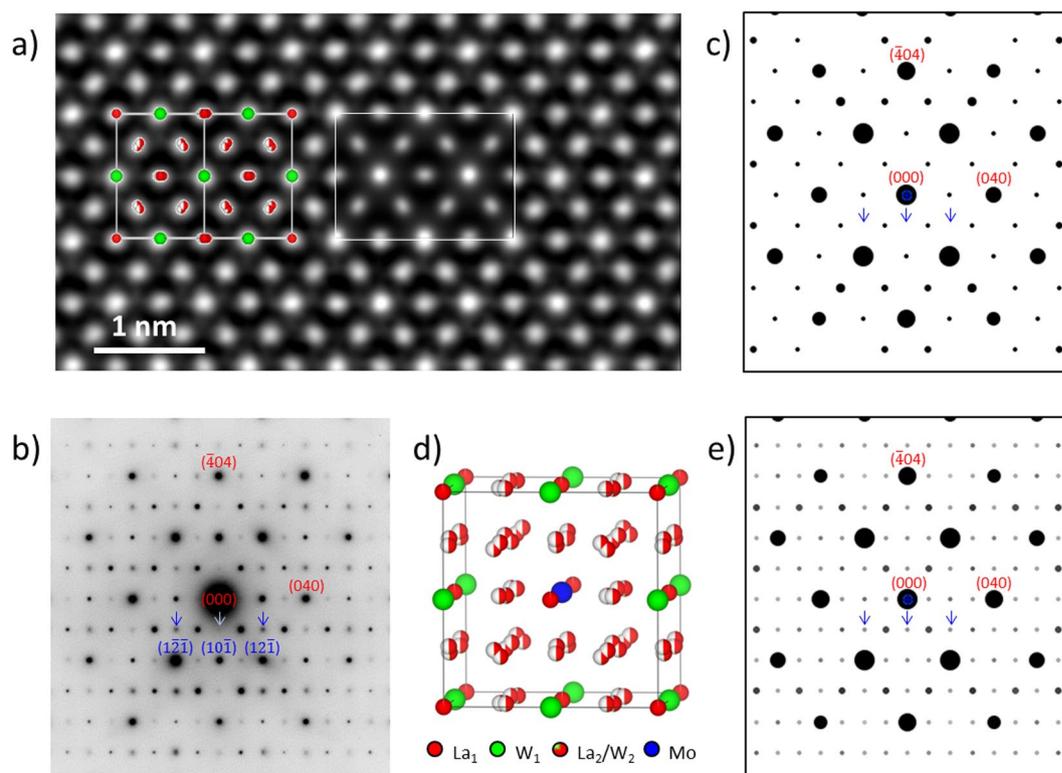


Figure 5. (a,b) HAADF image after averaging and smoothing, and diffraction pattern from LWO-Mo₃₅ recorded along [101] zone axis. The insets in (a) are an average LWO model and a simulated HAADF image based on the model. (c) Diffraction pattern simulated based on the average LWO model along [101]. (d) The average LWO model with the center W replaced by a Mo atom. (e) Simulated diffraction pattern based on the substituted model in (d) along [101]. The arrows are placed at equal positions in (b), (c) and (e).

the W_1 sites. For LWO, the structure factor, F_{La+W} , can be described as $F_{La+W} = \{f_{La} + f_W e^{\pi i(h+k+l)}\} \cdot F_{unit}$, where f_{La} and f_W are the atomic scattering amplitude for La and W atoms³⁰ respectively, h , k and l are the Miller indices, and $F_{unit} = 1 + e^{\pi i(h+k)} + e^{\pi i(h+l)} + e^{\pi i(k+l)}$. $F_{La+W} = 0$, if h , k and l are mixed odd and even. Thus, the extra reflections in Fig. 5b indexed as $(1\bar{2}1)$, $(10\bar{1})$ and $(12\bar{1})$ should be all forbidden. Successful Mo substitution revised F_{La+W} into $F_{La+W+Mo} = f_{La} \cdot F_{unit} + f_W e^{\pi i(h+k+l)} \cdot F_{unit} - f_W e^{\pi i(h+k+l)} + f_{Mo} e^{\pi i(h+k+l)}$, where f_{Mo} is the atomic scattering amplitude for Mo atoms. $F_{La+W+Mo} = \pm (f_W - f_{Mo})$, if h , k and l are mixed. As a result, reflections such as $(\bar{1}\bar{2}1)$, $(\bar{1}01)$ and $(\bar{1}21)$ with mixed Miller indices are allowed to appear, with an intensity proportional to $(f_{Mo} - f_W)^2$.

Comparing with LWO-Mo₂₀, there will be more Mo in LWO-Mo₃₅ contributing to the reflections with mixed Miller indices, which accounts for the generally stronger extra spots in the diffraction patterns from LWO-Mo₃₅, in Fig. 2f,h. One other feature noticed in the experimental patterns is the diffuse scattering, which also becomes stronger with higher Mo substitution, as depicted in Fig. 2 and Fig. S4. Similar diffuse scattering has been reported in some other good oxygen-ion conductors with a cubic fluorite structure, such as ceria and zirconia^{31,32}. In the lanthanide-doped ceria, the local ordering of oxygen vacancies develops with increasing doping level, and gives rise to stronger diffuse scattering. In addition, this development of ordering is found to be monotonously correlated with the degradation of ionic conductivity^{20,33}. For LWO, a higher La/W ratio indicates more oxygen vacancies, but a less stable structure^{14,34}. According to the EPMA results (Supplementary Table S1), LWO-Mo₃₅ shows a higher La/(W+Mo) ratio, implying more concentrated oxygen vacancies than LWO-Mo₂₀. Thus, within LWO-Mo₃₅ the oxygen vacancies are more likely to cluster and get ordered, and therefore account for the stronger diffuse scattering observed experimentally.

The average LWO model. Lanthanum tungstate was first believed to consist of La_6WO_{12} ³⁵ and only exists as a high temperature phase. Recent studies corrected this formula with a defected model, and mainly two (average) structural models were reported. Both of them describe the average crystal structure as an oxygen-deficient fluorite lattice, with doubling of the lattice parameter due to cation ordering. La_1 and W_1 form fcc lattices, and each La_1 and W_1 site is fully occupied and forms an octahedral environment with the surrounding oxygen atoms. The La_2 has a more distorted environment with an average oxygen coordination of seven. The nearest W_1 neighbors are linked by a La_2 site, and one additional W_2 sits on the La_2 site to stabilize the LWO phase. Depending on whether the La_2/W_2 sites are split and thus half occupied, one model belongs to the space group $Fm\bar{3}m$ ²⁵ and the other belongs to $F\bar{4}3m$ ^{14,16,36}. The split of La_2/W_2 sites is considered to be necessary to develop a structural model on a local level²⁵. Experimentally, studies based on synchrotron X-ray powder diffraction and neutron powder diffraction support the split model ($Fm\bar{3}m$) as a more accurate one than the non-split model ($F\bar{4}3m$)¹⁹. However, there is still no direct evidence thus far from TEM, to prove the split of La_2/W_2 sites.

Oriented along $[101]$ zone axis, Fig. 6a shows the split model with its $[12\bar{1}]$ direction pointing upwards. A rhombohedron and one of its diagonals are defined by the dotted lines there, and four atomic columns are labeled as i , ii , iii and iv . Resulting from the split of the La_2/W_2 site, atomic columns elongate either along the edges or the diagonals of the rhombohedron, like those labeled as i , ii and iii . For the columns like the one labeled as iv , the elongation is along the $[101]$ direction, and thus invisible under this condition. The HAADF image in Fig. 6b was recorded from LWO-Mo₂₀ along the $[101]$ zone axis. An $\sim 1.07 \times 1.38 \text{ nm}^2$ area, as marked by the square, is cropped out and compared with the rhombohedron in Fig. 6c. The same image is then color coded in Fig. 6d, where the shape of atomic columns is better revealed. Already, the asymmetric feature in column i , ii and iii can be noticed. Intensity profiles along the dotted pink and green lines were extracted and plotted in Fig. 6e for each atomic column. The pink/green lines are parallel/perpendicular to the edges and diagonal of the rhombohedron. A Gaussian fit was then carried out, to estimate the full width at half maxima (FWHM) for each curve in Fig. 6e. The estimated values from each atomic column along both directions are then compared in the lower right table. Taking column i for example, the difference between $d_{i,par}$ and $d_{i,per}$ is around 0.33 \AA , while for column iv , the $d_{iv,par}$ and $d_{iv,per}$ are almost the same (difference $\sim 0.01 \text{ \AA}$). Similarly, for column ii and iii , around 0.3 \AA difference between the parallel and perpendicular directions were determined. Thus, by HAADF imaging, the asymmetric elongation of atomic columns resulting from the La_2/W_2 site split is directly proven for the first time, which provides solid evidence for the accuracy of the split model.

Conclusions

In summary, our study has revealed the atomic structure of LWO with different amounts of Mo substitution. The average LWO model with split La_2/W_2 sites was proven to be more accurate to describe the crystal structure. EDX chemical mapping confirmed that Mo replaces W, and up to 35 at.% W replaced by Mo didn't affect the original fluorite structure of LWO. The different scattering factors of Mo and W resulted in extra reflections in the diffraction patterns from Mo-substituted LWOs. The diffuse scattering provided evidence of the clustering and short-range ordering of oxygen vacancies, which became stronger with higher Mo concentration.

Mo was introduced into LWO, aiming to improve the electrical conductivity of the membrane. However, this is accompanied with a side effect of ordering of oxygen vacancies at room temperature, which could degrade the membranes' ionic conductivity. To enhance the electrical conductivity while maintain an acceptable ionic conductivity as well as the stability of the system, a comprehensive study on the membrane performance, the Mo substitution and the LWO crystal structure after substitution would be necessary. The atomic structures identified in this work can be further connected with the gas separation performance, and provide a solid structural basis for thoroughly understanding the membranes' properties. Moreover, the Mo substitution shows the ability to alter the La/(W + Mo) ratio in a predictable way within a certain window, and additionally reduce the porosity of the membrane material. All these may in turn offer opportunities to rationally tailor the functional properties of the membranes by precise control of Mo content.

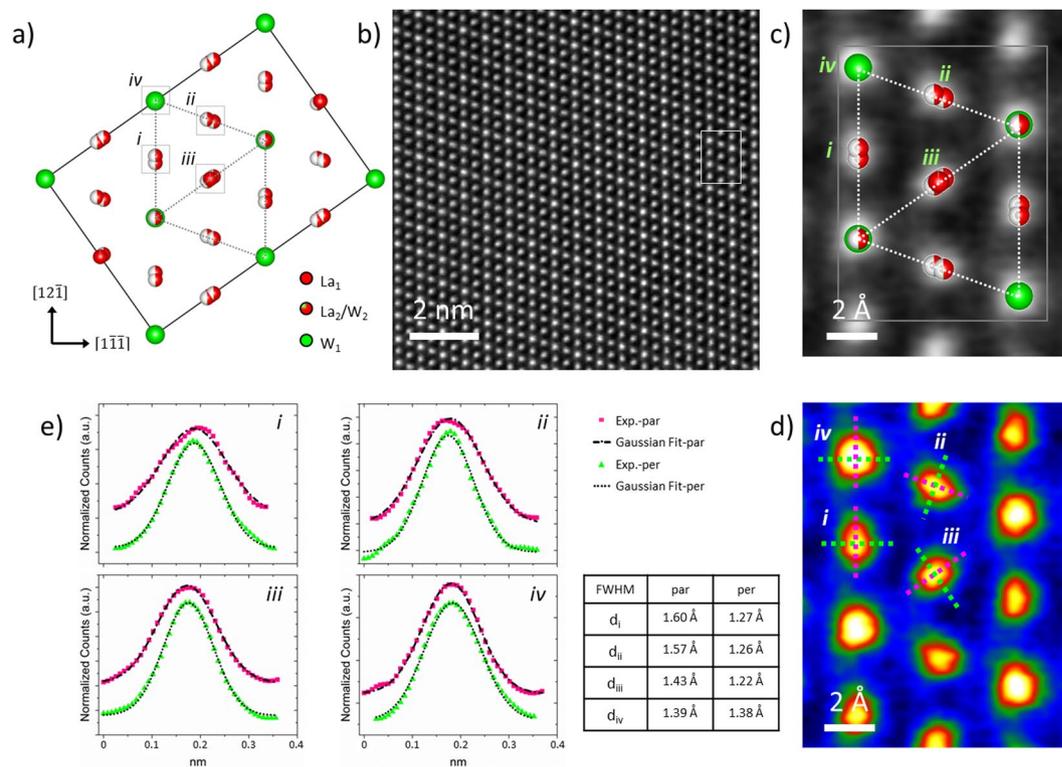


Figure 6. Measurement of the split of La_2/W_2 sites. (a) The average LWO model with split La_2/W_2 sites, oriented along $[101]$ zone axis. Four different types of atomic columns are labeled as *i*, *ii*, *iii* and *iv*. (b) HAADF image from LWO- Mo_{20} recorded along $[101]$ zone axis, after averaging and smoothing. (c) HAADF image cropped from the marked region in (b). The dotted rhombohedron in (a) is overlaid on the image for comparison. (d) The colored coded image of (c). The dotted pink/green lines are parallel/perpendicular to the edges and diagonal of the rhombohedron. (e) Intensity profiles extracted along the dotted lines in (d) for atomic columns *i* to *iv*, together with Gaussian fit results. The lower right table lists the full width at half maxima (FWHM) determined from Gaussian fit, for each atomic column along each direction.

Methods

Preparation of LWO with and without Mo substitution. The LWO material was prepared by a modified Pechini method²⁷. Lanthanum nitrate hexahydrate (Sigma Aldrich), ammonium tungstate (Sigma Aldrich) and ammonium molybdate (Sigma Aldrich) were used as the precursors. The complexation reaction was performed as shown in¹¹. The mixtures were calcined at 900 °C in air to remove the organic constituents and form an oxide. Afterwards, 1 gram of the powder was pressed to pellets with a diameter of 20 mm. The final sintering step was performed at 1500 °C for 12 h with heating rates of 5 K/min to obtain high densification and complete phase formation. XRD measurements were performed with a Bruker D4 X-ray diffractometer. The Mo concentration was varied between 0 and 35%, meaning that up to 35% of the W was substituted by Mo. Higher Mo concentrations appeared to be not stable after storage in air for several days.

TEM sample preparation. LWO pellets were first embedded in resin (Kulzer). After gradual grinding and polishing, cross section SEM samples with flat surfaces were prepared. Carbon coating was applied to reduce the possible charging problem during SEM imaging and EPMA measurement. TEM specimens were cut from the cross section SEM samples by focused ion beam (FIB) milling using an FEI Helios NanoLab 400 S system with a Ga ion beam³⁷. Further thinning and cleaning were performed with an Ar ion beam in a Fischione Nanomill 1040 at 900 and 500 eV beam energy respectively.

Characterization techniques. SEM and EPMA measurements were carried out on a JEOL JSM7000F and a CAMEBAX SX 50 instrument, respectively. Electron diffraction was performed on a FEI Tecnai F20 at 200 kV. High resolution HAADF imaging was conducted with an FEI Titan 80–300 STEM³⁸ and an FEI Titan G2 80–200 ChemiSTEM³⁹ microscope operated at 300 kV and 200 kV, respectively. Atomic resolution EDX chemical mapping was performed on an FEI Titan G2 80-200 ChemiSTEM microscope equipped with an XFEG, a probe C_s corrector and a super-X EDXS system. The convergence semi-angle for STEM imaging and EDX chemical mapping was approximately 22 mrad, while the collection semi-angle was 88–200 mrad for HAADF imaging. EDX maps were collected typically for ~10 minutes, and background subtraction was performed following the steps previously described⁴⁰. STEM HAADF image simulations were performed with the Dr. Probe software package⁴¹. Aberrations were not taken into account in the simulations since this work was not aimed on full quantifying the experimental images. Structural models were visualized with VESTA⁴². Electron diffraction patterns were simulated by the JEMS software.

References

- Ivanova, M. E. *et al.* Hydrogen separation through tailored dual phase membranes with nominal composition $\text{BaCe}_{0.8}\text{Eu}_{0.2}\text{O}_{3-\delta}\text{Ce}_{0.8}\text{Y}_{0.2}\text{O}_{2-\delta}$ at intermediate temperatures. *Sci. Rep.* **6**, 34773 (2016).
- Escolastico, S., Solis, C., Scherb, T., Schumacher, G. & Serra, J. M. Hydrogen separation in $\text{La}_{5.5}\text{WO}_{11.25-\delta}$ membranes. *J. Membrane Sci.* **444**, 276–284 (2013).
- Escolastico, S., Solis, C., Kjolseth, C. & Serra, J. M. Outstanding hydrogen permeation through CO_2 -stable dual-phase ceramic membranes. *Energ. Environ. Sci.* **7**, 3736–3746 (2014).
- Czyperek, M. *et al.* MEM-BRAIN gas separation membranes for zero-emission fossil power plants. *Energy Proced.* **1**, 303–310 (2009).
- Czyperek, M. *et al.* Gas separation membranes for zero-emission fossil power plants: MEM-BRAIN. *J. Membrane Sci.* **359**, 149–159 (2010).
- Iwahara, H., Uchida, H., Ono, K. & Ogaki, K. Proton Conduction in Sintered Oxides Based on BaCeO_3 . *J. Electrochem. Soc.* **135**, 529–533 (1988).
- Hamakawa, S., Li, L., Li, A. & Iglesia, E. Synthesis and hydrogen permeation properties of membranes based on dense $\text{SrCe}_{0.95}\text{Yb}_{0.05}\text{O}_{3-\delta}$ thin films. *Solid State Ionics* **148**, 71–81 (2002).
- Wei, X. T., Kniep, J. & Lin, Y. S. Hydrogen permeation through terbium doped strontium cerate membranes enabled by presence of reducing gas in the downstream. *J. Membrane Sci.* **345**, 201–206 (2009).
- Bohn, H. G. & Schober, T. Electrical conductivity of the high-temperature proton conductor $\text{BaZr}_{0.9}\text{Y}_{0.1}\text{O}_{2.95}$. *J. Am. Ceram. Soc.* **83**, 768–772 (2000).
- Escolastico, S. *et al.* Improvement of transport properties and hydrogen permeation of chemically-stable proton-conducting oxides based on the system $\text{BaZr}_{1-x-y}\text{Y}_x\text{M}_y\text{O}_{3-\delta}$. *Rsc. Adv.* **2**, 4932–4943 (2012).
- Seeger, J. *et al.* Synthesis and characterization of nonsubstituted and substituted proton-conducting $\text{La}_{6-x}\text{WO}_{12-y}$. *Inorg. Chem.* **52**, 10375–10386 (2013).
- Escolastico, S., Solis, C. & Serra, J. M. Hydrogen separation and stability study of ceramic membranes based on the system $\text{Nd}_5\text{LnWO}_{12}$. *Int. J. Hydrogen Energy* **36**, 11946–11954 (2011).
- Escolastico, S., Solis, C. & Serra, J. M. Study of hydrogen permeation in $(\text{La}_{5/6}\text{Nd}_{1/6})_{5.5}\text{WO}_{12-\delta}$ membranes. *Solid State Ionics* **216**, 31–35 (2012).
- Magrasso, A. *et al.* Complete structural model for lanthanum tungstate: a chemically stable high temperature proton conductor by means of intrinsic defects. *J. Mater. Chem.* **22**, 1762–1764 (2012).
- Fantin, A. *et al.* Crystal structure of Re-substituted lanthanum tungstate $\text{La}_{5.4}\text{W}_{1-y}\text{Re}_y\text{O}_{12-\delta}$ ($0 < y < 0.2$) studied by neutron diffraction. *J. Appl. Crystallogr.* **49**, 1544–1560 (2016).
- Magrasso, A., Frontera, C., Marrero-Lopez, D. & Nunez, P. New crystal structure and characterization of lanthanum tungstate “ $\text{La}_6\text{WO}_{12}$ ” prepared by freeze-drying synthesis. *Dalton T.* 10273–10283 (2009).
- Magrasso, A. & Haugsrud, R. Effects of the La/W ratio and doping on the structure, defect structure, stability and functional properties of proton-conducting lanthanum tungstate $\text{La}_{28-x}\text{W}_{4+x}\text{O}_{54+\delta}$. A review. *J. Mater. Chem. A* **2**, 12630–12641 (2014).
- Ivanova, M. *et al.* Influence of the $\text{La}_6\text{W}_2\text{O}_{15}$ phase on the properties and integrity of $\text{La}_{6-x}\text{WO}_{12-\delta}$ -based membranes. *Chemistry and Materials Research* **2** (2012).
- Magrasso, A. & Frontera, C. Comparison of the local and the average crystal structure of proton conducting lanthanum tungstate and the influence of molybdenum substitution. *Dalton T* **45**, 3791–3797 (2016).
- Amsif, M. *et al.* Mo-Substituted lanthanum tungstate $\text{La}_{28-y}\text{W}_{4+y}\text{O}_{54+\delta}$: a competitive mixed electron-proton conductor for gas separation membrane applications. *Chem. Mater.* **24**, 3868–3877 (2012).
- Escolastico, S. *et al.* Enhanced H_2 separation through mixed proton-electron conducting membranes based on $\text{La}_{5.5}\text{W}_{0.8}\text{M}_{0.2}\text{O}_{11.25-\delta}$. *Chemoschem* **6**, 1523–1532 (2013).
- Deibert, W., Ivanova, M. E., Meulenberg, W. A., Vassen, R. & Guillon, O. Preparation and sintering behaviour of $\text{La}_{5.4}\text{WO}_{12-\delta}$ asymmetric membranes with optimised microstructure for hydrogen separation. *J. Membrane Sci.* **492**, 439–451 (2015).
- Deibert, W. *et al.* Stability and sintering of MgO as a substrate material for Lanthanum Tungstate membranes. *J. Eur. Ceram. Soc.* **37**, 671–677 (2017).
- Stournari, V. *et al.* Mechanical properties of tape casted Lanthanum Tungstate for membrane substrate application. *Ceram. Int.* **42**, 15177–15182 (2016).
- Scherb, T. *et al.* Nanoscale order in the frustrated mixed conductor $\text{La}_{5.6}\text{WO}_{12-\delta}$. *J. Appl. Crystallogr.* **49**, 997–1008 (2016).
- Fantin, A. *et al.* Relation between composition and vacant oxygen sites in the mixed ionic electronic conductors $\text{La}_{5.4}\text{W}_{1-y}\text{M}_y\text{O}_{12-\delta}$ ($\text{M} = \text{Mo}, \text{Re}; 0 < y < 0.2$) and their mother compound $\text{La}_{6-x}\text{WO}_{12-\delta}$ ($0.4 < x < 0.8$). *Solid State Ionics* **306**, 104–111 (2017).
- Escolastico, S., Vert, V. B. & Serra, J. M. Preparation and characterization of nanocrystalline mixed proton-electronic conducting materials based on the system $\text{Ln}_6\text{WO}_{12}$. *Chem. Mater.* **21**, 3079–3089 (2009).
- Magrasso, A. *et al.* *In situ* high temperature powder neutron diffraction study of undoped and Ca-doped $\text{La}_{28-x}\text{W}_{4+x}\text{O}_{54+3x/2}$ ($x = 0.85$). *J. Mater. Chem. A* **1**, 3774–3782 (2013).
- Du, H. A nonlinear filtering algorithm for denoising HR(S)TEM micrographs. *Ultramicroscopy* **151**, 62–67 (2015).
- Ibers, J. A. Atomic scattering amplitudes for electrons. *Acta Crystallogr.* **11**, 178–183 (1958).
- Garcia-Martin, S., Alario-Franco, M. A., Fagg, D. P., Feighery, A. J. & Irvine, J. T. S. Modulated fluorite-type structure of materials from the $(1-x)\text{Y}_{0.5}\text{Zr}_{0.5}\text{O}_{1.75-x}\text{Y}_{0.75}\text{Nb}_{0.25}\text{O}_{1.75}$ ($0 < x < 1$) system. *Chem. Mater.* **12**, 1729–1737 (2000).
- Ye, F., Mori, T., Ou, D. R., Zou, J. & Drennan, J. Microstructural characterization of terbium-doped ceria. *Mater. Res. Bull.* **42**, 943–949 (2007).
- Ou, D. R. *et al.* Oxygen-vacancy ordering in lanthanide-doped ceria: dopant-type dependence and structure model. *Phys. Rev. B* **77**, 024108-1-8 (2008).
- Erdal, S. *et al.* Defect structure and its nomenclature for mixed conducting lanthanum tungstates $\text{La}_{28-x}\text{W}_{4+x}\text{O}_{54+3x/2}$. *Int. J. Hydrogen Energy* **37**, 8051–8055 (2012).
- Yoshimura, M. & Baumard, J. F. Electrical-conductivity of solid-solutions in system $\text{CeO}_2\text{-La}_6\text{WO}_{12}$. *Mater. Res. Bull.* **10**, 983–988 (1975).
- Kalland, L. E., Magrasso, A., Mancini, A., Tealdi, C. & Malavasi, L. Local structure of proton-conducting lanthanum tungstate $\text{La}_{28-x}\text{W}_{4+x}\text{O}_{54+\delta}$: a combined density functional theory and pair distribution function study. *Chem. Mater.* **25**, 2378–2384 (2013).
- Meertens, D., Kruth, M. & Tillmann, K. FEI Helios NanoLab 400S FIB-SEM. *Journal of large-scale research facilities* **2**, A60 (2016).
- Heggen, M., Lusyberg, M. & Tillmann, K. FEI Titan 80-300 STEM. *Journal of large-scale research facilities* **2**, A42 (2016).
- Kovács, A., Schierholz, R. & Tillmann, K. FEI Titan G2 80-200 CREWLEY. *Journal of large-scale research facilities* **2**, A43 (2016).
- Williams, D. B. & Carter, C. B. *Transmission Electron Microscopy: A Textbook for Materials Science*. (Springer, 2009).
- Barthel, J. Dr. Probe: A software for high-resolution STEM image simulation. *Ultramicroscopy* **193**, 1–11 (2018).
- Momma, K. & Izumi, F. VESTA 3 for three-dimensional visualization of crystal, volumetric and morphology data. *J. Appl. Crystallogr.* **44**, 1272–1276 (2011).

Acknowledgements

We acknowledge support from the Bundesministerium für Bildung und Forschung (BMBF) under the Grant ProtOMem (03SF0537A and 03SF0537B). We thank Maximilian Kruth for preparation of the TEM lamellae by FIB, Fabian Mariano for SEM measurement, Christian von Lechberg for EPMA measurement, and Riza Iskandar, Lei Jin and Daesung Park for helpful discussion.

Author Contributions

W.D. prepared the LWO membrane materials. K.R. performed the experimental electron microscopy and image simulations. K.R. and J.M. interpreted the experimental results and wrote the manuscript. M.E.I., W.A.M. and J.M. supervised the research. All the authors discussed the results and commented on the manuscript.

Additional Information

Supplementary information accompanies this paper at <https://doi.org/10.1038/s41598-019-39758-2>.

Competing Interests: The authors declare no competing interests.

Publisher's note: Springer Nature remains neutral with regard to jurisdictional claims in published maps and institutional affiliations.



Open Access This article is licensed under a Creative Commons Attribution 4.0 International License, which permits use, sharing, adaptation, distribution and reproduction in any medium or format, as long as you give appropriate credit to the original author(s) and the source, provide a link to the Creative Commons license, and indicate if changes were made. The images or other third party material in this article are included in the article's Creative Commons license, unless indicated otherwise in a credit line to the material. If material is not included in the article's Creative Commons license and your intended use is not permitted by statutory regulation or exceeds the permitted use, you will need to obtain permission directly from the copyright holder. To view a copy of this license, visit <http://creativecommons.org/licenses/by/4.0/>.

© The Author(s) 2019